Japanese Journal of Applied Physics

The Japan Society of Applied Physics

REGULAR PAPER

Acceleration of lithotripsy using cavitation bubbles induced by second-harmonic superimposition

To cite this article: Masamizu Osuga *et al* 2016 *Jpn. J. Appl. Phys.* **55** 07KF18

Japanese Journal of Applied Physics **55**, 07KF18 (2016)
http://doi.org/10.7567/JJAP.55.07KF18

REGULAR PAPER

Acceleration of lithotripsy using cavitation bubbles induced by second-harmonic superimposition

Masamizu Osuga[1*], Jun Yasuda[1], Hayato Jimbo[1], Shin Yoshizawa[1*], and Shin-ichiro Umemura[2]

[1]Graduate School of Engineering, Tohoku University, Sendai 980-8579, Japan
[2]Graduate School of Biomedical Engineering, Tohoku University, Sendai 980-8579, Japan

*E-mail: m_osuga@ecei.tohoku.ac.jp; syoshi@ecei.tohoku.ac.jp

Received November 15, 2015; accepted March 25, 2016; published online June 21, 2016

Shock wave lithotripsy potentially produces residual stone fragments too large to pass through ureters and significant injury to the normal tissue surrounding the stone. Previous works have shown that the collapse of cavitation bubbles induced by high-intensity focused ultrasound can produce small stone fragments via cavitation erosion. However, the erosion rate is hypothesized to be reduced by ultrasound attenuation by excessively generated bubble clouds. If so, it is important to generate the bubbles only on the stone surface. The effects of peak-negative-enhanced (PNE) and peak-positive-enhanced (PPE) waves obtained by second-harmonic superimposition were investigated to control cavitation bubbles. With the PNE waves, the bubbles were generated only on the stone surface and the maximum erosion rate was 232 ± 32 mg/min. All the fragments were smaller than 2 mm, which makes them pass through ureters naturally. The proposed method shows the potential to significantly improve the speed of lithotripsy.

1. Introduction

Shock wave lithotripsy (SWL) has been one of the several first-line treatments for shattering kidney stones. In this treatment technique, several dozens of MPa shock waves of ~1 µs duration are focused into the kidney stone from outside the body to shatter that stone. Thus, SWL is a noninvasive treatment technique needing no surgical incision. However, it has some problems. Firstly, it suffers from the fact that it tends to produce residual stone fragments too large to pass through ureters.[1–5] Secondly, injuries of the surrounding kidney tissue, apparently caused by cavitation, have also been reported.[6,7] Cavitation bubbles are generated in a region larger than a kidney stone and injure the surrounding normal tissue because the shock wave used in SWL has a focal region larger than the stone.[8] Although the cavitation phenomenon is a factor of injuries to a normal tissue, cavitation bubbles have important mechanisms of shattering the stone.[9–14] For example, the high pressure inside the bubbles contributes to shattering the kidney stone treated by lithotripsy into smaller fragments.[15,16]

High-intensity focused ultrasound (HIFU) is a noninvasive treatment method, in which ultrasound is generated outside the body and its energy is focused onto a target tissue. In the focal region of HIFU, acoustic cavitation bubbles can be generated by a highly negative pressure due to focusing. Ikeda and coworkers[17,18] reported that using the collapse of cavitation bubbles caused by HIFU resulted in the production of small stone fragments from disruption because, in this method, the stone is shattered as if it is scraped into small fragments like powder via cavitation erosion. In addition, the frequency used in HIFU treatment, which is typically about 1 MHz, is much higher than that in SWL. Hence, the injuries to a normal tissue surrounding the stone are much less severe than those in SWL because the focusing ability of the energy is much higher and the focal region is much smaller in the HIFU method than in SWL.[19] However, the erosion rate of the proposed method is significantly lower than that of SWL, which is considered as the problem of the method. In 2006, the erosion rate achieved by Ikeda and coworkers using HIFU was about 10 mg/min.[17,18] By using a peak negative pressure that is about threefold higher and a pulse reputation frequency (PRF) that is 40-fold higher than those of Ikeda et al.,[17] the erosion rate was improved to about 90 mg/min in accordance with the results achieved by Duryea and coworkers in 2011.[5,20] However, this rate is approximately 80% of that of piezoelectric SWL,[5] whose erosion rate is relatively lower than those of other types of SWL.

The erosion rate is hypothesized to be significantly reduced by ultrasound attenuation due to the excessive generation of bubble clouds. It has been reported that the erosion rate does not markedly increase with the size of bubble clouds in the propagation direction of ultrasound at a high peak negative pressure.[20] This result indicates that it is important to generate the bubbles only on the stone surface in order to improve the erosion rate. Although the peak negative pressure triggers the generation of acoustic cavitation bubbles and stimulates their oscillation and expansion, it was shown that the peak positive pressure of the focused ultrasound has a significant role in generating bubble clouds.[21] Second-harmonic superimposition is investigated to enhance the cavitation effect in sonodynamic therapy[22] and thermotherapy,[23] to localize the cavitation region[24] and generate cavitation bubbles efficiently.[25,26] The second-harmonic superimposition can obtain either peak-negative-enhanced (PNE) or peak-positive-enhanced (PPE) waves by adjusting the amplitude and phase of the second harmonic. Yoshizawa et al. demonstrated on a surface of an aluminum block that the behavior of cavitation bubbles and clouds can be controlled by using PPE and PNE waves, both of which can be obtained by superimposing the second harmonic to the fundamental.[19] They observed that the cavitation bubbles were generated only on the aluminum surface by PNE waves, while bubble clouds were generated from the stone surface and then extended toward the transducer in the case of PNE waves followed by PPE waves.

The objective of this study is to improve the erosion rate of lithotripsy using cavitation bubbles induced by second-harmonic superimposed ultrasound pulses. The behaviors of cavitation bubbles and bubble clouds were observed using a high-speed camera when the fundamental, PNE, and PPE waves were focused onto a stone surface, and model stones

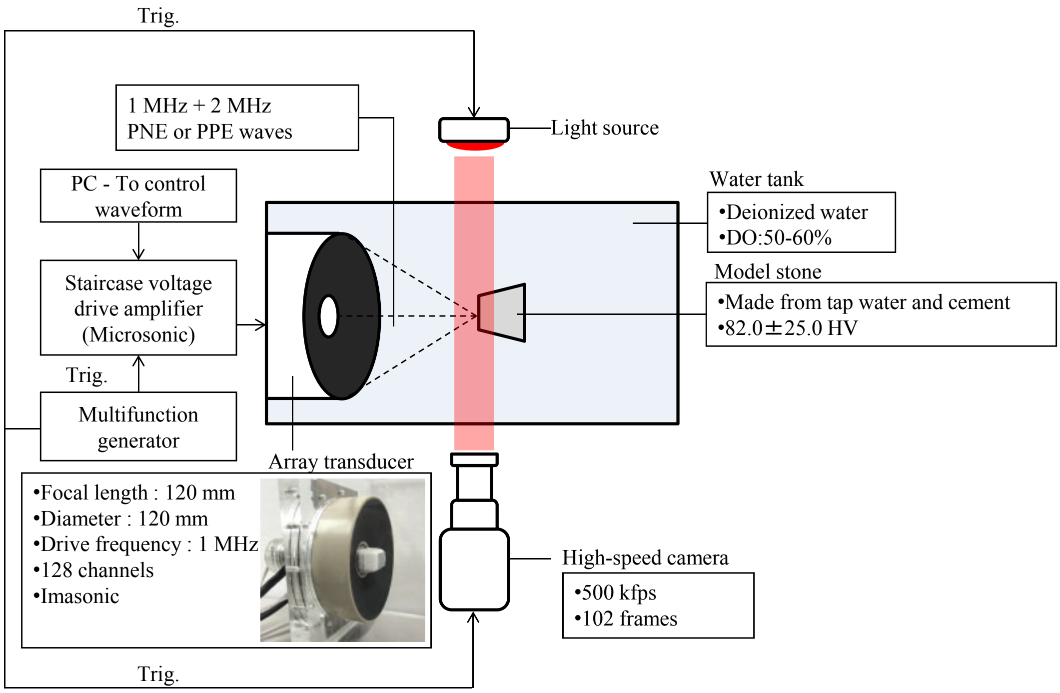

Fig. 1. (Color online) Schematic of experimental setup.

made from cement were eroded by focusing these waves. Subsequently, the erosion rate of model stones was measured and compared between the cases of using these waves and, in the present study, the feasibility of using second-harmonic superimposition to erode kidney stones was evaluated.

2. Experimental methods

2.1 Model kidney stones

Model stones[27] were made from tap water and commercially available cement powder (Katei Kagaku Kogyo), which is used to repair concrete cracks. Dry cement powder was calmly mixed with tap water at the ratio of 10 : 6 (g: mL) for 10 min. Subsequently, an aliquot of the slurry was poured into a mold. After 72 h, the stones were removed from the mold. The size of model stones on the focal plane of HIFU was $12 \times 12\,\mathrm{mm}^2$ and the length in the HIFU propagation direction was about 15 mm. The average dehydrated weight of the stones was 4.49 ± 0.27 g (mean $\pm$ SD, n = 180). Vickers hardness has a correlation with the erosion resistance of materials.[28] It was measured for the surface to be treated before sonication using a microindentation tester (Shimadzu HMV-G21) with a load of 50 g. Five stones were randomly chosen for the measurement. Vickers hardness is expressed as

$$HV = 1854 \cdot (P/d^2), \tag{1}$$

where HV is the Vickers hardness in kg/mm^2, P is the load of the diamond indenter in g, and d is the impressed diagonal length on the surface in µm. The average hardness was determined to be 82.0 ± 25.0 HV, which is consistent with the reported values of the natural and model stones.[29] After sonication, the stones were dried for 72 h to remove the water from them to calculate the erosion rate. The erosion rate was calculated as

$$R_e = \frac{m_b - m_a}{\Delta t}, \tag{2}$$

where R_e is the erosion rate, m_b and m_a are the weights before and after sonication, respectively, and Δt is the sonication time.

2.2 Experimental setup

Figure 1 shows a schematic of the experimental setup. A 128-element concave array ultrasound transducer (Imasonic) was placed in a water tank filled with deionized water. The geometric focal length is 120 mm and the outer and inner diameters are 120 and 40 mm, respectively. The transducer was designed to have a dual-peak efficiency at 1 and 2 MHz by using a heavy acoustic impedance matching layer.[30,31] Such an efficiency was measured by a force balance method to be 85.4 and 61.9% at those frequencies, respectively. A model stone was degassed by a vacuum desiccator (AS ONE VE-ALL) for 5 h to decrease the amount of remaining gas in the stone. Firstly, the model stones were put in a beaker filled with degassed water. Secondly, the stones and beaker were set in the vacuum desiccator at −70 kPa. Then, a model stone was fixed at the focus of HIFU. The water was filtered through an activated carbon filter and a 0.45 µm mesh filter and then deionized. The temperature and dissolved oxygen (DO) level ranged from 20 to 30 °C and from 3.5 to 4.5 mg/L, respectively. This DO level was consistent with the reported values in human urine.[32] A high-speed camera (Shimadzu HPV-2A) was set to observe the behavior of cavitation bubbles generated on the stone surface at a frame rate of 500 kfps and an exposure time of 250 ns with a lens system (Leica Z16 APO). The resolution of the camera was 312 (horizontal) × 260 (vertical) pixels. One pixel corresponded to $20 \times 20\,\mu\mathrm{m}^2$ in the following experiments. The light source was a laser light source (CAVILUX Smart; wavelength: 690 nm; maximum pulse output power: 400 W), which illuminated for 20 ns during each exposure of the camera.

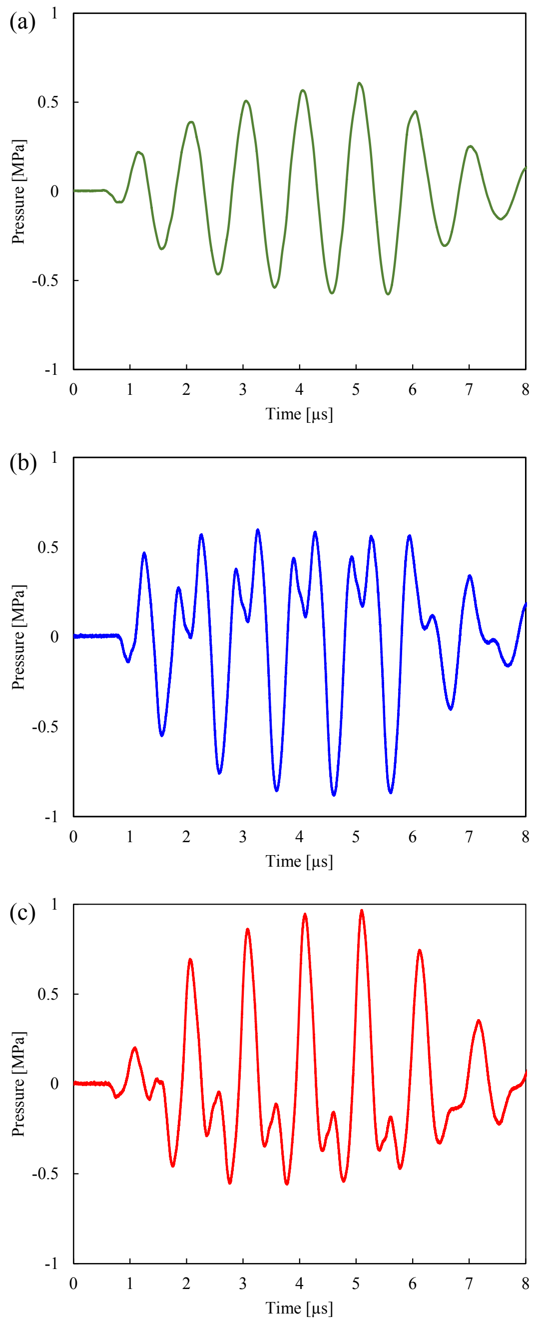

Fig. 2. (Color online) (a) Fundamental, (b) PNE waves, and (c) PPE waves at the ultrasound focus at a TAP of 0.6 W.

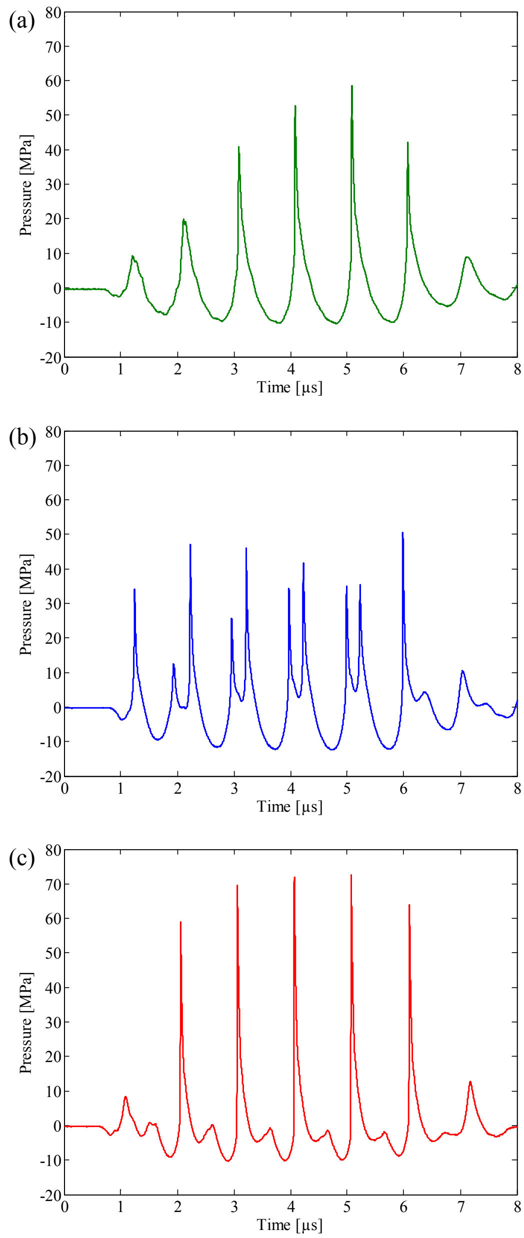

Fig. 3. (Color online) (a) Fundamental, (b) PNE waves, and (c) PPE waves at the ultrasound focus at a TAP of 300 W.

2.3 Waveforms and sequences

The second-harmonic superimposed pressure waveform at a low intensity can be written as[22)]

$$p = p_1 \cos \omega t + p_2 \cos(2\omega t + \varphi), \tag{3}$$

where p_1 and p_2 are the amplitudes of the fundamental and second harmonic, respectively. φ is the phase difference between the second harmonic and the fundamental, which was set at π and 0 for the PNE and PPE waves, respectively. In this study, the fundamental and second-harmonic frequencies were 1 and 2 MHz, respectively. They were chosen because the electric impedance of the transducer was reasonably small at the two frequencies. The p_2/p_1 ratio was set to 0.6, which resulted in the ratios of the peak positive pressure to the peak negative pressure $p_+/|p_-|$ of approximately 1 : 2 and 2 : 1 in the PNE and PPE waves, respectively. The p_2/p_1 ratio and φ were tuned by measuring the focal pressure with a capsule hydrophone (Onda HGL-0085). Figures 2(a)–2(c) show the pressure waveforms of the fundamental, PNE, and PPE waves at the focus at a total acoustic power (TAP) of 0.6 W, respectively. In addition, Figs. 3(a)–3(c) show those at a TAP of 300 W, respectively. They were measured with the capsule hydrophone and a fiber optic hydrophone (Onda HFO-660) at the TAPs of 0.6 and 300 W, respectively. The TAPs of 0.01, 0.06, 0.16, 0.38, and 0.61 W were calculated from the pressure field on the focal plane measured with the capsule hydrophone when the PPE waves were exposed. The TAP of 300 W was estimated from these TAPs, assuming that the TAP increases proportionally to the input electric power.

Figure 4 shows ultrasound exposure sequences in this study. Each pulse lasted 5 µs at a TAP of 300 W and was stopped for 10 µs before the next pulse, considering the

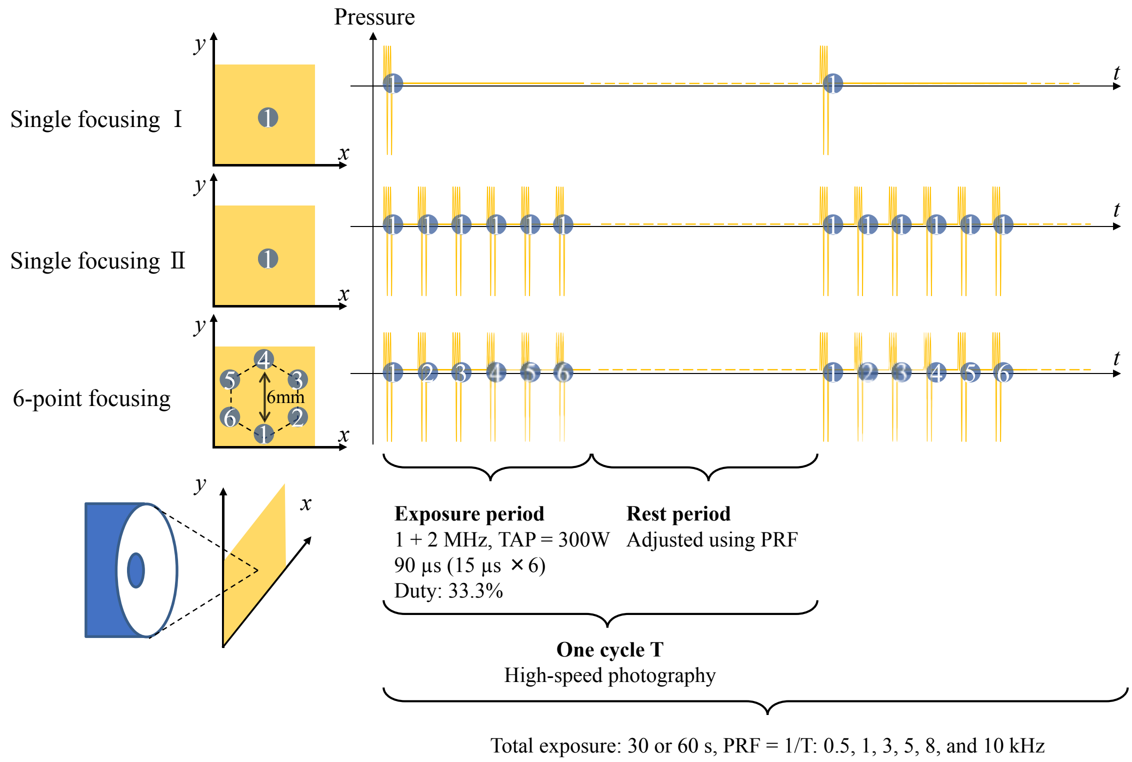

Fig. 4. (Color online) Schematic of ultrasound sequence.

thermal load on the amplifiers. In this study, three ultrasound sequences were tested. The first sequence was "single focusing I". The pulse wave was irradiated onto the geometric focus of HIFU only once in a sequence cycle. The second sequence was "single focusing II". The pulse wave was consecutively irradiated sixfold onto the geometric focus. The third sequence was "6-point focusing". The pulse wave was electronically scanned sequentially with the array transducer at each apex of a regular hexagon at the focal plane by utilizing the performance of the array transducer. The single focusing II and 6-point focusing result in an overall sequence duration of 90 μs. The PRF of all sequences was varied by adjusting the rest period between consecutive sequences. All sequences were repeated for 30 and 60 s at PRFs of 0.5, 1, 3, 5, 8, and 10 kHz. High-speed photographs were taken during the first exposure period of all sequences.

3. Results

3.1 High-speed camera images

High-speed optical images near the model stone during the exposure period of all sequences at a TAP of 300 W are shown in Figs. 5–7. The black square on the right of each image is the shadow of the model stone. Ultrasound propagated from left to right in each figure.

The images in the case of the single focusing I sequence are shown in Figs. 5(a)–5(c). In all cases of the fundamental, PNE, and PPE waves, small bubble clouds started to be generated on the stone surface at the same time that ultrasound reached there. The bubble clouds almost disappeared in 60 to 72 μs. Compared with the PNE waves, the PPE waves generated bubble clouds significantly closer to the transducer as shown in Figs. 5(b) and 5(c) in all of the ten experiments. Additionally, the fundamental also tended to generate bubble clouds significantly closer to the transducer

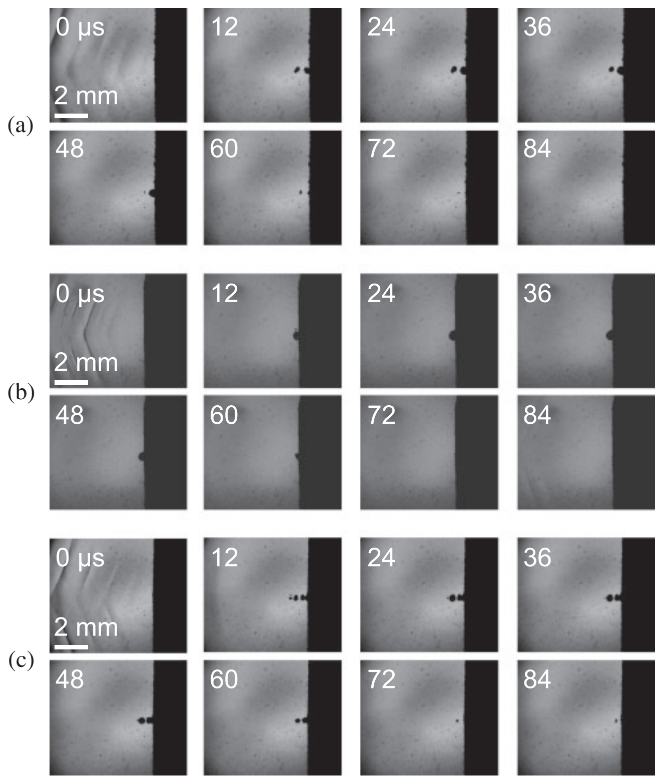

Fig. 5. High-speed images of the region near the model stone at a TAP of 300 W in the case of single focusing I: (a) fundamental, (b) PNE waves, and (c) PPE waves.

compared with the PNE waves as shown in Figs. 5(a) and 5(b) in seven of the ten experiments. In four other experiments, the size of the bubble clouds of the fundamental was almost the same as that of the PNE waves.

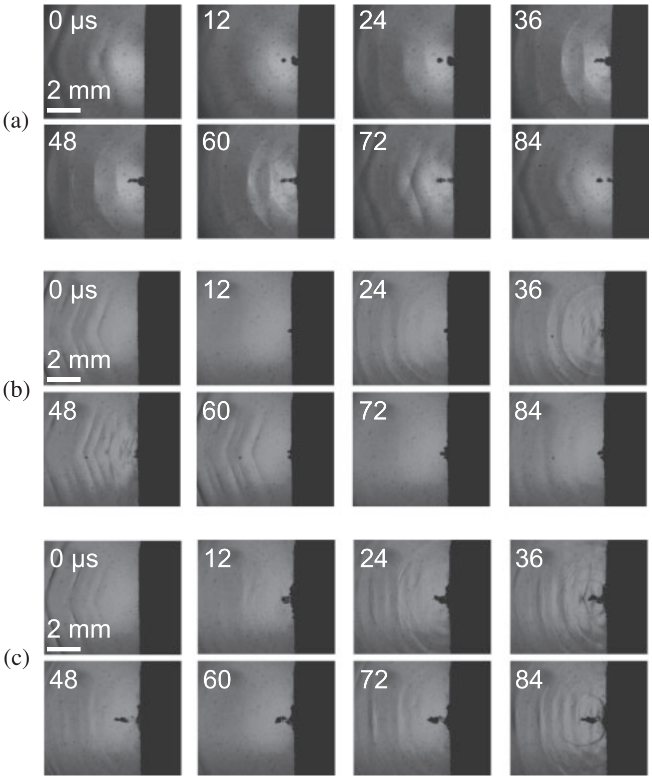

Fig. 6. High-speed images of the region near the model stone at a TAP of 300 W in the case of single focusing II: (a) fundamental, (b) PNE waves, and (c) PPE waves.

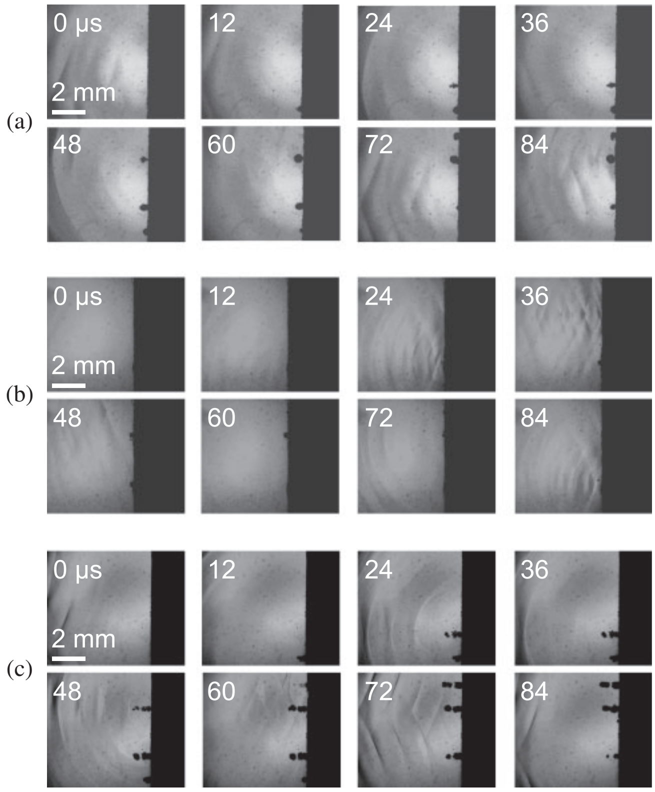

Fig. 7. High-speed images of the region near the model stone at a TAP of 300 W in the case of 6-point focusing: (a) fundamental, (b) PNE waves, and (c) PPE waves.

The images in the case of the single focusing II sequence are shown in Figs. 6(a)–6(c). The bubbles and bubble clouds did not disappear throughout a cycle since ultrasound was continuously irradiated before the bubbles generated by the previous pulse disappeared. Particularly in the case of the PPE waves, cavitation bubbles were generated on the stone first and then a cavitation cloud was generated and expanded toward the transducer, as shown in Fig. 6(c), in all of the ten experiments.

The images in the case of the 6-point focusing sequence are shown in Figs. 7(a)–7(c). The state of the bubbles and bubble clouds generated sequentially at each hexagonal apex can be observed for all waves. With the fundamental and PPE waves, cavitation clouds expanded toward the transducer, while with the PNE waves, cavitation bubbles remained only on the stone surface. Compared with the PNE waves, the PPE waves generated bubble clouds significantly closer to the transducer, as shown in Figs. 7(b) and 7(c), in all of the ten experiments. Additionally, the fundamental also tended to generate bubble clouds significantly closer to the transducer compared with the PNE waves, as shown in Figs. 7(a) and 7(b), in nine of the ten experiments. In the remaining experiment, the size of the bubble clouds of the fundamental was almost the same as that of the PNE waves.

3.2 Erosion rate measurements

Figures 8–10 show the stone erosion rate plotted as a function of PRF in the cases of single focusing I, single focusing II, and 6-point focusing, respectively. The number of eroded stones was 5 under each condition of the waveforms, sequences, and PRFs. In the case of single focusing I, the erosion rates of both waves tend to increase

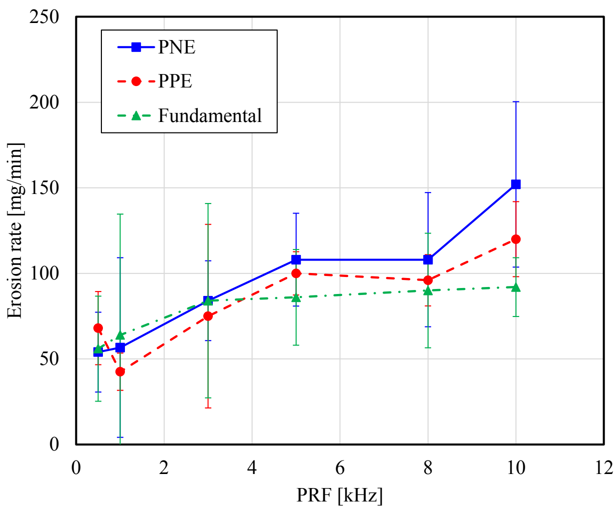

Fig. 8. (Color online) Stone erosion rate plotted as a function of PRF in the case of single focusing I.

at all the PRFs. The maximum average erosion rate was 152.0 ± 48.3 mg/min at the PRF of 10 kHz in the case of PNE waves. The erosion rates of all waves saturated in the PRF range from 5 to 10 kHz with the single focusing II sequence. The maximum average erosion rate of this sequence was 124.0 ± 59.9 mg/min at the PRF of 10 kHz in the case of PNE waves. When the 6-point focusing sequence was used, the erosion rate of the PNE waves increased at all the PRFs, while that of the PPE waves saturated in the PRF range from 5 to 10 kHz. The maximum average erosion rate was 232.0 ± 31.9 mg/min at the PRF of 10 kHz in the case of PNE waves.

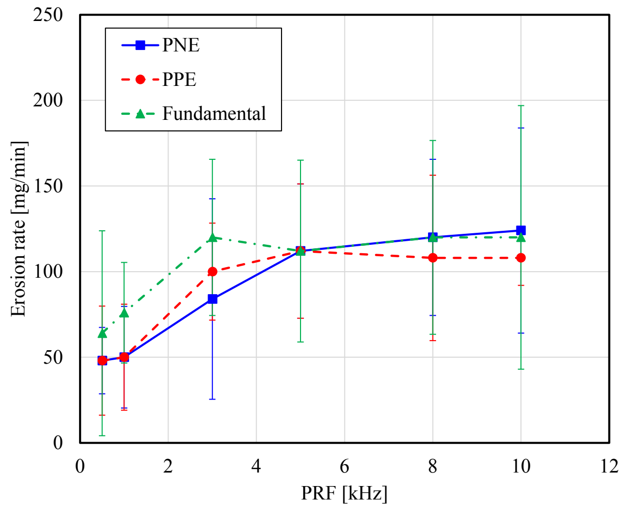

Fig. 9. (Color online) Stone erosion rate plotted as a function of PRF in the case of single focusing II.

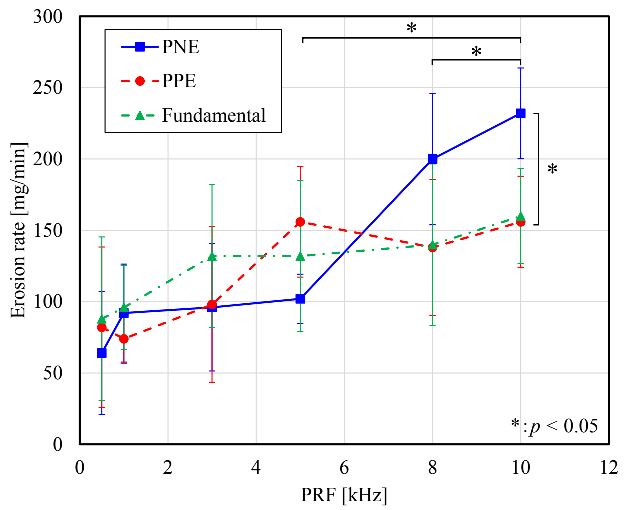

Fig. 10. (Color online) Stone erosion rate plotted as a function of PRF in the case of 6-point focusing.

3.3 Size of eroded fragments

Figures 11 and 12 show the pictures of residual stone fragments produced by HIFU disruption and the equivalent diameter distribution of erosion fragments. The equivalent diameter is calculated from the binary-processed image of the photographed eroded fragments with ImageJ for each particle. The equivalent diameter was calculated as

$$D_e = \frac{4S}{l}, \tag{4}$$

where D_e is the equivalent diameter, S is the area of the particle, and l is the peripheral length of the particle. The mean diameters were 0.28 ± 0.07 mm for 1220 particles and 0.27 ± 0.01 mm for 1101 particles, and the largest particle diameters were 0.69 and 0.86 mm for the PNE and PPE waves, respectively.

4. Discussion

It has been reported that a positive pressure is an important factor for bubble cloud formation.[21] The waveform at a focus of HIFU is distorted so as to have an extremely highly peak

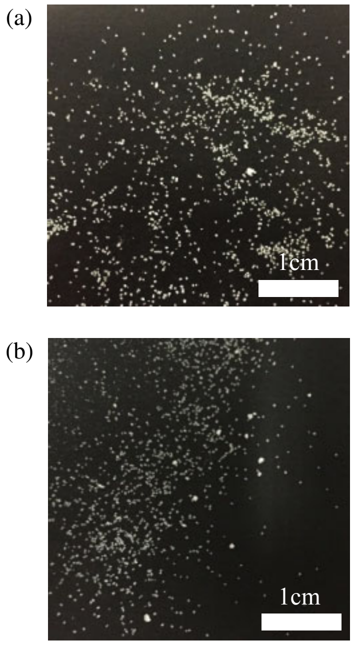

Fig. 11. (Color online) Residual stone fragments produced by disruption in the cases of the (a) PNE and (b) PPE waves.

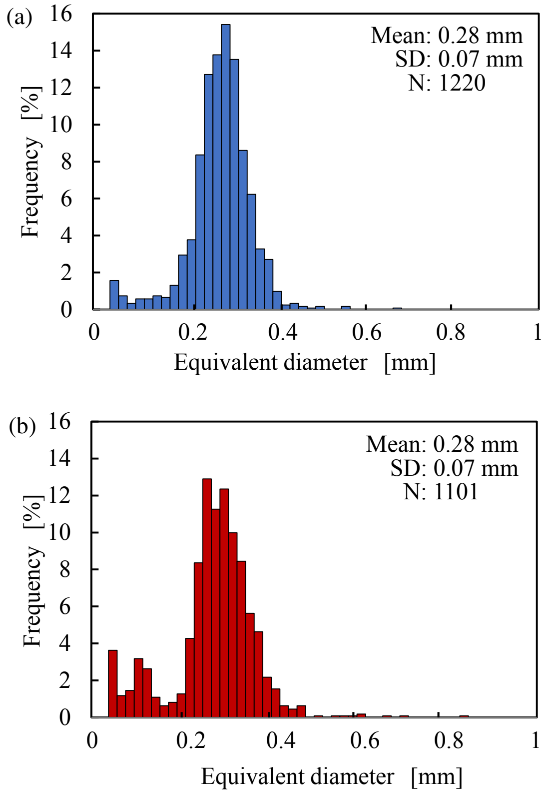

Fig. 12. (Color online) Size frequency of number size distribution of fragment diameter in the cases of the (a) PNE and (b) PPE waves.

positive pressure[33,34] owing to nonlinear propagation followed by focal phase shift. When the waves with a nonlinearly distorted waveform were incident on bubbles, the extremely highly positive pressure was phase-inverted with respect to the incident wave on the surface of bubbles. This is because the bubbles had a pressure-releasing surface. This phase inversion will result in a highly negative pressure wave propagating back toward the transducer. This highly negative pressure will generate a bubble cluster, forming a bubble cloud. The following positive pressure part of the next cycle will be scattered by the cluster and expanded to a larger bubble cloud. Thus, the higher the positive peak of a waveform is, the larger the generated bubble cloud is. The waveforms of the fundamental, PNE, and PPE waves used in the experiment were also distorted by nonlinear propagation as shown in Figs. 3(a)–3(c), respectively. The maximum peak positive pressures were approximately 60, 50, and 70 MPa, respectively. The peak positive pressure of the PNE waves was suppressed compared with that of the PPE waves at the focus, although the TAPs of all the waves were the same. Thus, in accordance with the cloud formation mechanism,[21] the cavitation bubbles and clouds should tend to be suppressed in the case of the PNE waves. In Figs. 5–7, it can be shown that bubble cloud formation was suppressed in the case of the PNE waves compared with the fundamental and PPE waves.

As shown in Figs. 8 and 9, the maximum erosion rates of all single focusing sequences were almost the same, although the exposure time of single focusing II was sixfold as long as that of single focusing I. In addition, cavitation bubbles or clouds did not disappear and covered the stone surface throughout the exposure period as shown in the high-speed photographs in Figs. 6(a)–6(c). These results and photographs indicate that the cavitation clouds covered and shielded the stone surface. The first pulse wave of a cycle generated the cavitation bubbles or clouds on the stone surface and eroded the surface via cavitation erosion. However, even though the second or more pulse waves were supplied to the stone, the surface was not further eroded unless the bubbles and bubble clouds disappear before the next pulse was supplied. This shielding effect of bubble clouds can also be suggested from the other finding. The erosion rate of single focusing I tends to increase, while that of the single focusing II tends to saturate at higher PRFs from 5 to 10 kHz. The interval time before each first pulse in a cycle in single focusing II is shorter than that in single focusing I because single focusing II has six pulses in an exposure cycle. The interval times of single focusing I were 120 and 95 μs at 8 and 10 kHz, while those of single focusing II were 35 and 10 μs at 8 and 10 kHz, respectively. From Figs. 5(a)–5(c), cavitation bubbles and clouds, generated by a pulse, need about 70 μs to perfectly disappear. Therefore, at these PRFs, the next cycle seems to have started before the cavitation clouds disappeared and the bubbles remained on the stone surface shielding the sonication of the next cycle in single focusing II. The bubble clouds continued to exist and cover the stone when the next exposure cycle started. Hence, even when the PRF was increased, the erosion rate did not increase.

There are small differences between the average erosion rates of two single focusing sequences and the 6-point focusing sequence at low PRFs. However, the average erosion rates of 6-point focusing were higher than those of both single focusing sequences at high PRFs from 8 to 10 kHz for all waves. 6-point focusing did not cause overlapping of cavitation bubbles because the bubbles and bubble clouds generated at each focus had sufficient time to disappear during the scanning of the focus to other focal points. Therefore, all the pulses of a cycle were successfully

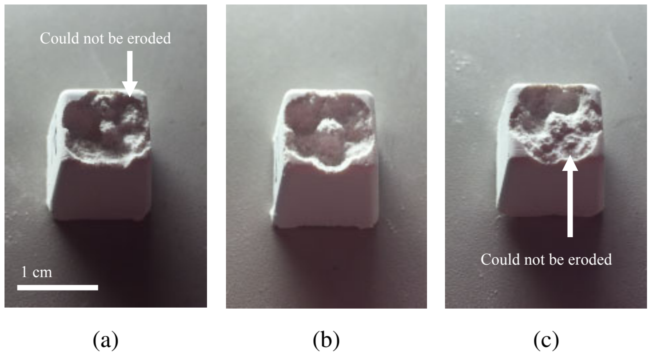

Fig. 13. (Color online) Pictures of model stones after eroding using (a) fundamental, (b) PNE, and (c) PPE waves with 6-point focusing at 5 kHz.

conducted without being shielded by bubble clouds. The erosion rate of the PNE waves increased at all PRFs, while those of the fundamental and PPE waves tended to saturate at high PRFs. This is because the shielding effect of cavitation bubbles and clouds may not have occurred even at high PRFs in the case of the PNE waves because the PNE waves generate bubbles only on the stone surface as shown in Figs. 7(a)–7(c). On the other hand, a bubble cloud can be easily expanded toward the transducer when using the fundamental and PPE waves compared with the case of the PNE waves. Hence, ultrasound pulse propagation was shielded by the clouds, and the erosion rates of the fundamental and PPE waves tended to saturate at high PRFs. P-values between the erosion rates of the PNE waves at a PRF of 10 kHz and the other waves at PRFs of 5, 8, and 10 kHz were calculated to investigate the significance of using the PNE waves at high PRFs, and the results are shown in Fig. 10. The p-values were lower than 0.05 at all PRFs. Thus, the difference between the PNE waves and the other waves was more significant at higher PRFs.

The erosion rate achieved by Ikeda et al. using HIFU was about 10 mg/min.[17,18] In addition, the erosion rate of lithotripsy using histotripsy pulses was about 90 mg/min and that using piezoelectric SWL was about 110 mg/min, in accordance with the results of Duryea and coworkers.[5,20] The erosion rate achieved by the PNE waves at 10 kHz was more than twofold higher than these rates from the literature. In these studies, the model stone made from Ultracal-30 gypsum-based cement[27] was used. The Vickers hardness of the model stones measured by Ikeda et al. was 56.4 ± 16.9 HV,[17] which is lower than the value of the model stones used in this study. Hence, it can be considered that the erosion rate achieved by this study is significantly higher than those obtained by previous studies.

Figures 13(a)–13(c) show the pictures of the model stone after being eroded by the fundamental, PNE, and PPE waves with 6-point focusing at 5 kHz, respectively. Figure 13(b) shows that the stone could be eroded evenly at all focal points with the PNE waves. All the stones were eroded similarly. On the other hand, Figs. 13(a) and 13(c) show that the stone could not be eroded finely at some of the focal points either with the fundamental or PPE waves. These traces of erosion could be confirmed for about half of the stones. This is also because the shielding phenomenon of bubbles was prevented at all focal points by the PNE waves. Hence, it can be considered that the PNE waves can consistently erode the stone at all focal points, but the fundamental and PPE waves may erode the stone unevenly.

From the results of the size distribution of eroded fragments, all fragments eroded with the PNE and PPE waves were smaller than 2 mm by an order of magnitude. Traditional clinical perspective deems erosion fragments less than 2 mm as clinically insignificant because they are likely to dispose naturally through ureters with minimal difficulty.[20] Being eroded by cavitation erosion, the stones could be scraped and eroded finely from the surface. Hence, the erosion of stones via cavitation erosion has an advantage in making the stone fragments fine in lithotripsy.

5. Conclusions

In this study, a method of shattering model kidney stones by the collapse of cavitation bubbles induced by second-harmonic superimposed HIFU was investigated. The behavior of the cavitation bubbles near the surface of a model stone in a HIFU focal region was observed using a high-speed camera. The erosion rate was measured after the stones were eroded using cavitation bubbles induced by second-harmonic superimposition. A multiple focusing sequence gave a higher erosion rate than single focusing sequences. The erosion rate of the PNE waves increased at all PRFs, while those of the fundamental and PPE waves tended to saturate at high PRFs. The maximum erosion rate reached approximately 250 mg/min, which is much higher than the results of several previous works, i.e., more than twofold. These are probably because the shielding phenomenon of bubble clouds could be suppressed by reducing the size of the clouds with the PNE waves in the propagation direction of HIFU. The PNE waves have an advantage in that they improve the erosion rate at a high PRF compared with that in the case of only the fundamental or PNE waves. In addition, all the fragments were smaller than 2 mm, which will make them pass through ureters naturally. Although further studies are needed to optimize the sequence and evaluate the feasibility to erode various kinds of stones, the second-harmonic superimposition has a potential to significantly improve the erosion rate of lithotripsy.

Acknowledgments

This research was partially supported by the Research and Development of Advanced Medical Devices and Systems to Achieve the Future of Medicine/Development of a Smart Treatment Chamber for the Improvement of Both Medical Safety and Efficiency from the Japan Agency for Medical Research and Development, AMED.

1) T. B. Mobley, D. A. Myers, W. B. Grine, J. M. Jenkins, and W. R. Jordan, J. Urol. **149**, 1419 (1993).
2) T. G. Liston, B. S. Montgomery, M. I. Bultitude, and R. C. Tiptaft, Br. J. Urol. **69**, 465 (1992).
3) F. Coz, M. Orvieto, M. Bustos, R. Lyng, C. Stein, A. Hinrichs, and I. San Francisco, J. Endourology **14**, 239 (2000).
4) A. S. Cass, J. Urol. **153**, 588 (1995).
5) A. P. Duryea, T. L. Hall, A. D. Maxwell, Z. Xu, C. A. Cain, and W. W. Roberts, J. Endourology **25**, 341 (2011).
6) A. P. Evan, L. R. Willis, J. A. Mcateer, M. R. Bailey, B. A. Connors, Y. Shao, J. E. Lingeman, J. C. Williams, N. S. Fineberg, and L. A. Crum, J. Urol. **168**, 1556 (2002).
7) M. Derius, G. Enders, Z. Xuan, H. G. Liebich, and W. Brendel, Ultrasound Med. Biol. **14**, 117 (1998).
8) C. Chaussy, G. Haupt, D. Jocham, K. U. Köhrmann, and D. Wilbert, *Therapeutic Energy Application in Urology: Standards and Recent Developments* (Georg Thieme Verlag, Stuttgart, 2005) p. 26.
9) X. Xi and P. Zhong, Ultrasound Med. Biol. **26**, 457 (2000).
10) A. J. Coleman and J. E. Saunders, Ultrasound Med. Biol. **13**, 69 (1987).
11) M. B. Bailey, L. N. Couret, O. A. Sapozhnikov, V. A. Khokhlova, G. T. Haar, S. Vazey, X. Shi, R. Martin, and L. A. Crum, Ultrasound Med. Biol. **27**, 695 (2001).
12) D. Cathignol, J. Tavakkoli, A. Birer, and A. Arefiev, IEEE Trans. Ultrason. Ferroelectr. Freq. Control **45**, 788 (1998).
13) Y. A. Pishchalnikov, O. A. Sapozhnikov, M. R. Baily, J. C. Williams, R. O. Cleveland, T. Colonius, L. A. Crum, A. P. Evan, and J. A. Mcateer, J. Endourology **17**, 435 (2003).
14) A. P. Duryea, W. W. Roberts, C. A. Cain, and T. L. Hall, IEEE Trans. Ultrason. Ferroelectr. Freq. Control **60**, 301 (2013).
15) D. L. Sokolov, M. R. Baielly, and L. A. Crum, J. Acoust. Soc. Am. **110**, 1685 (2001).
16) S. Zhu, F. H. Cocks, G. M. Preminger, and P. Zhong, Ultrasound Med. Biol. **28**, 661 (2002).
17) T. Ikeda, S. Yoshizawa, M. Tosaki, J. S. Allen, S. Takagi, N. Ohta, T. Kitamura, and Y. Matsumoto, Ultrasound Med. Biol. **32**, 1383 (2006).
18) S. Yoshizawa, T. Ikeda, A. Ito, R. Ota, S. Takagi, and Y. Matsumoto, Med. Biol. Eng. Comput. **47**, 851 (2009).
19) S. Yoshizawa, J. Yasuda, and S. Umemura, J. Acoust. Soc. Am. **134**, 1515 (2013).
20) A. P. Duryea, A. D. Maxwell, W. W. Roberts, Z. Xu, T. L. Hall, and C. A. Cain, IEEE Trans. Ultrason. Ferroelectr. Freq. Control **58**, 971 (2011).
21) A. D. Maxwell, T. Wang, C. A. Cain, and Z. Xu, J. Acoust. Soc. Am. **130**, 1888 (2011).
22) S. Umemura, K. Kawabata, and K. Sasaki, J. Acoust. Soc. Am. **101**, 569 (1997).
23) H. Sasaki, J. Yasuda, R. Takagi, T. Miyashita, K. Goto, S. Yoshizawa, and S. Umemura, Jpn. J. Appl. Phys. **53**, 07KF11 (2014).
24) S. D. Sokka, T. P. Gauthier, and K. Hynynen, Phys. Med. Biol. **50**, 2167 (2005).
25) J. Yasuda, A. Asai, S. Yoshizawa, and S. Umemura, Jpn. J. Appl. Phys. **52**, 07HF11 (2013).
26) R. Takagi, S. Yoshizawa, and S. Umemura, Jpn. J. Appl. Phys. **50**, 07HF14 (2011).
27) J. A. McAteer, J. C. Williams, Jr., R. O. Cleveland, J. Van Cauwelaert, M. R. Bailey, D. A. Lifshitz, and A. P. Evan, Urol. Res. **33**, 429 (2005).
28) S. Hattori, R. Ishikura, and Q. Zhang, Wear **257**, 1022 (2004).
29) D. Heimbach, R. Munver, P. Zhong, J. Jacobs, A. Hesse, S. C. Muller, and G. M. Preminger, J. Urol. **164**, 537 (2000).
30) Y. Qian and N. R. Harris, Ultrasonics **54**, 586 (2014).
31) Z. Zaini, S. Umemura, H. Jimbo, R. Takagi, and S. Yoshizawa, Proc. IEEE Int. Ultrasonics Symp., 2015, P5C3-3.
32) X. Giannakopoulos, A. Evangelou, V. Kalfakakou, E. Grammeniatis, I. Papandropoulos, and K. Charalambopoulos, Int. Urol. Nephrol. **29**, 393 (1997).
33) M. S. Canney, M. R. Bailey, L. A. Crum, V. A. Khokhlova, and O. A. Sapozhnikov, J. Acoust. Soc. Am. **124**, 2406 (2008).
34) J. E. Parsons, C. A. Cain, and J. B. Fowlkes, J. Acoust. Soc. Am. **119**, 1432 (2006).